Extreme Mechanics Letters 77 (2025) 102315

Contents lists available at ScienceDirect

Extreme Mechanics Letters

journal homepage: www.elsevier.com/locate/eml

Piezoelectric gauge transformation for inverse design of polar Willis transducers

Li Huang [a], Rui Zhu [b,*], Gengkai Hu [b], Yangyang Chen [a,*]

[a] Department of Mechanical and Aerospace Engineering, The Hong Kong University of Science and Technology, Clear Water Bay, Hong Kong
[b] School of Aerospace Engineering, Beijing Institute of Technology, Beijing 100081, China

ARTICLE INFO

Keywords:
Transformation elasticity
Lattice metamaterials
Piezoelectric transducers
Displacement control

ABSTRACT

Piezoelectric lattices with delicately designed microscopic geometry are powerful building blocks to construct integrated sensors and actuators with versatile, yet unconventional, responses absent from bulk materials. However, the inverse design of the microscopic geometry to achieve a sought-after electromechanical response remains elusive. Here, we suggest an analytical approach, called *piezoelectric gauge transformation*, to design piezoelectric lattice transducers that can deform to an arbitrary desired displacement field when a voltage is applied. We first develop continuum piezoelectric gauge transformation and find that the transformed piezoelectric material displays piezoelectric polarity and Willis coupling in the sense that the applied electric field generates asymmetric stress and body force, and both rigid body rotation and translation induce electric charges. To design this polar and Willis-type piezoelectric material, we develop discrete piezoelectric gauge transformation and propose feasible lattice design guidelines. Numerical simulations are performed to validate the piezoelectric gauge transformation and demonstrate a range of appealing displacement control functions. The study presents a complete theoretical framework for the inverse design of lattice transducers to achieve arbitrary desired actuated displacement fields, beneficial to the development of soft actuators, robotics, and other piezoelectric devices.

1. Introduction

Designing piezoelectric materials with desired electromechanical responses is a key issue of fundamental importance for the application of piezoelectric devices ranging from, traditionally, sonar systems [1,2], pressure and force sensors [3,4], ultrasonic actuators [5,6], energy harvesters [7,8], medical imaging [9,10], clock generators [11,12], and scanning probe microscopes [13,14], to, currently, soft electronics [15,16], soft robotics [17,18], sustainable technologies [19,20], and precise as well as personalized medical devices [21–24]. Often, electromechanical properties and responses of piezoelectric materials are determined by their crystallographic structures and compositions [25]. Different techniques (e.g. doping) have been suggested to change crystallographic structures to control properties of piezoelectric materials. However, limitations still exist, e.g. coupled mechanical flexibility and sensitivity and a narrow range of piezoelectric anisotropy [26,27]. Recent breakthroughs in additive manufacturing allow the construction of three-dimensional, and multi-material, piezoelectric lattices composed of a set of small piezoelectric beams on the microscopic scale [28–30]. The geometric degrees of freedom on the fabricable microscopic scale enlarge the design space of piezoelectric properties and responses in a way similar to that of mechanical metamaterials [31–33]. Some nonstandard electromechanical properties and responses absent in bulk materials (e.g. designed anisotropy and directional response) have been demonstrated in piezoelectric lattices [34–36]. However, the inverse design of piezoelectric lattices to achieve desired electromechanical responses remains elusive. On one hand, the solution of the inverse problem is not guaranteed to be unique or stable. On the other hand, the inverse design of piezoelectric lattices involves complex interaction between elasticity and electricity.

Here, we suggest a simple analytical approach to design piezoelectric lattice transducers that can deform to a desired displacement field under a given electric voltage (see Fig. 1a). The analytical approach is formulated by extending transformation elasticity to transformation piezoelectricity. Transformation elasticity, widely known for the design of elastic cloaks, builds the equivalency between the change in curvilinear coordinates and the change in material parameters [37–39]. Since its discovery, transformation elasticity has been an efficient tool for calculating material parameters to control the wave trajectories described by the change in coordinates. Unlike transformation optics and acoustics, the form of the transformed constitutive relations in

* Corresponding authors.
E-mail addresses: ruizhu@bit.edu.cn (R. Zhu), maeychen@ust.hk (Y. Chen).

https://doi.org/10.1016/j.eml.2025.102315
Received 12 December 2024; Received in revised form 10 March 2025; Accepted 11 March 2025
Available online 22 March 2025

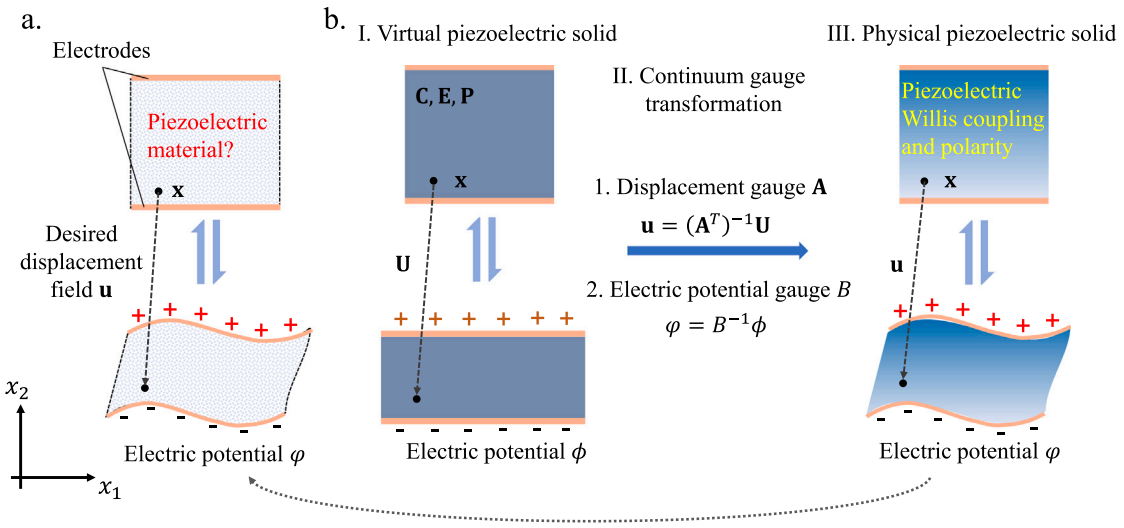

Fig. 1. Schematic representation of continuum piezoelectric gauge transformation for the inverse design of piezoelectric materials. (a) The goal of the inverse design is to calculate piezoelectric material parameters to achieve the desired displacement field with the application of an electric field. (b) During the inverse design, we first assume a piezoelectric material in the virtual space and calculate the displacement field with the application of an electric field. Based on the desired displacement field, we find the corresponding displacement and electric potential gauges. The required piezoelectric material parameters are solved by implementing continuum piezoelectric gauge transformation. The design piezoelectric material will display the desired displacement field automatically.

elasticity depends on the displacement gauge implemented during the transformation. For example, using the Milton–Brian–Willis gauge, the transformed constitutive relations display Willis coupling, where the stress is symmetric, but couples with velocity [37,38,40]. On the other hand, for the Brun–Guenneau–Movchan gauge, Willis coupling disappears, but the stress becomes asymmetric, and the elasticity tensor lacks minor symmetry [41–47]. It is worth mentioning that although the two gauges are common for cloaking and wave control purposes, the displacement gauge is not limited to the two, which, actually, can be arbitrary and manipulated intentionally. In particular, imposing the displacement gauge as a design variable, while keeping the coordinates the same during transformation, allows the control of displacement fields in solid materials at will [38,48]. This specific version of transformation elasticity is called gauge transformation. Remarkably, the materials for displacement control with a general displacement gauge display Willis coupling and polar properties at the same time. To design this polar Willis material, a discrete version of the gauge transformation has been suggested, where the transformation is operated among discrete lattices, rather than the continuum medium considered in conventional transformation methods [39,48,49]. However, what nonstandard piezoelectric properties arise when employing gauge transformation in piezoelectricity and how to implement discrete transformation to design piezoelectric lattice transducers to achieve a desired displacement field under a given electric voltage are still unknown.

In this study, we first operate the gauge transformation, by considering both the displacement gauge and the electric potential gauge, over a continuum piezoelectric material to calculate the electromechanical properties of the transformed piezoelectric solid for achieving a desired displacement field when the transformed piezoelectric solid is excited with the given electric voltage. We critically analyze the origin and consequences of polarity and Willis coupling in piezoelectricity as a result of the transformation. To design the polar and Willis-type piezoelectric materials, we perform the discrete gauge transformation over piezoelectric lattices. On the basis of the discrete piezoelectric gauge transformation, a lattice design guideline is suggested to construct the geometry of desired polar Willis piezoelectric lattices. Numerical simulations are performed to validate both the continuum and the discrete piezoelectric gauge transformations. Finally, we show procedures and examples of inverse design of lattice transducers to achieve the desired shape changes and strain fields under a given electric voltage. The study presents an analytical approach to guide the inverse design of lattice transducers, beneficial to the design of soft actuators, robotics, and other piezoelectric devices.

2. Piezoelectric gauge transformation

In this section, we formulate the continuum piezoelectric gauge transformation to calculate the electromechanical properties of the transformed piezoelectric materials. In the transformation, both the displacement and electric potential gauges are implemented. We consider a virtual piezoelectric solid occupied in $\mathbf{x}$ (see the left panel in Fig. 1b). The piezoelectric solid has the stiffness tensor $\mathbf{C}$, dielectric tensor $\mathbf{P}$ and piezoelectric tensor $\mathbf{E}$, which are defined as

$$T_{ij} = C_{ijkl}\frac{\partial U_l}{\partial x_k} + E_{ijk}\frac{\partial \phi}{\partial x_k}, \tag{1}$$

$$D_k = E_{ijk}\frac{\partial U_j}{\partial x_i} - P_{kl}\frac{\partial \phi}{\partial x_l}, \tag{2}$$

where T_{ij}, D_i, U_i, and ϕ denote the Cauchy stress tensor, electric displacement, displacement, and electric potential of the virtual piezoelectric solid, respectively. Note that the virtual piezoelectric solid is free-standing and absent from body torque, such that the stress tensor is symmetric $T_{ij} = T_{ji}$, and the stiffness and piezoelectric tensors hold minor symmetry, $C_{ijkl} = C_{jikl} = C_{jilk}$ and $E_{ijk} = E_{jik}$. In general, the displacement U_i can be determined from the equations of motion when an electric voltage is applied to the virtual piezoelectric solid together with a set of mechanical boundary conditions. To perform the gauge transformation, we calculate the potential energy density of the virtual piezoelectric solid, which reads as

$$\Xi = \frac{1}{2}C_{ijkl}\frac{\partial U_j}{\partial x_i}\frac{\partial U_l}{\partial x_k} - \frac{1}{2}P_{kl}\frac{\partial \phi}{\partial x_k}\frac{\partial \phi}{\partial x_l} + E_{ijk}\frac{\partial U_j}{\partial x_i}\frac{\partial \phi}{\partial x_k}. \tag{3}$$

Note that kinetic energy of the piezoelectric material is ignored in the derivations for simplicity. Thus, the results presented in the study can be a good approximation for quasi-static and low-frequency applications.

To achieve the desired displacement field $\mathbf{u}(\mathbf{x})$ under an electric potential field $\varphi(\mathbf{x})$ in the physical (or transformed) piezoelectric solid, we introduce two gauge fields (see the middle panel in Fig. 1b). One is the displacement gauge $\mathbf{A}(\mathbf{x})$, where $\mathbf{u} = \left(\mathbf{A}^T\right)^{-1}\mathbf{U}$. The other is the

electric potential gauge $B(\mathbf{x})$, where $\varphi = B^{-1}\phi$. As a result, the spatial gradients of the displacement and the electric potential read

$$\frac{\partial U_j}{\partial x_i} = A_{qj}\frac{\partial u_q}{\partial x_i} + \frac{\partial A_{qj}}{\partial x_i}u_q, \tag{4}$$

$$\frac{\partial \phi}{\partial x_k} = B\frac{\partial \varphi}{\partial x_k} + \frac{\partial B}{\partial x_k}\varphi. \tag{5}$$

Next, we let the potential energy density conserve before and after the transformation by substituting Eqs. (4) and (5) into Eq. (3), which leads to

$$\begin{aligned}\xi = \Xi = {} & \frac{1}{2}\left[C_{ijkl}\left(A_{ql}\frac{\partial u_q}{\partial x_k} + \frac{\partial A_{ql}}{\partial x_k}u_q\right) + E_{ijk}\left(B\frac{\partial \varphi}{\partial x_k} + \frac{\partial B}{\partial x_k}\varphi\right)\right] \\ & \times \left(A_{qj}\frac{\partial u_q}{\partial x_i} + \frac{\partial A_{qj}}{\partial x_i}u_q\right) \\ & + \frac{1}{2}\left[E_{ijk}\left(A_{qj}\frac{\partial u_q}{\partial x_i} + \frac{\partial A_{qj}}{\partial x_i}u_q\right) - P_{kl}\left(B\frac{\partial \varphi}{\partial x_l} + \frac{\partial B}{\partial x_l}\varphi\right)\right] \\ & \times \left(B\frac{\partial \varphi}{\partial x_k} + \frac{\partial B}{\partial x_k}\varphi\right).\end{aligned} \tag{6}$$

Clearly, the transformed potential energy density depends not only on the displacement gradient $\frac{\partial u_j}{\partial x_i}$ and the electric field $\frac{\partial \varphi}{\partial x_i}$, but also on the displacement u_i and the electric potential φ. By taking derivatives of the transformed potential energy density ξ with respect to the gradient of displacement $\frac{\partial u_j}{\partial x_i}$, the displacement u_i, the electric field $\frac{\partial \varphi}{\partial x_i}$, and the electric potential φ, we can obtain the formulas of stress, body force, electric displacement, and charge density per volume in the transformed piezoelectric material, respectively, as

$$\sigma_{ij} = c_{ijkl}\frac{\partial u_l}{\partial x_k} + s_{ijk}u_k + e_{ijl}\frac{\partial \varphi}{\partial x_l} + g_{ij}\varphi, \tag{7}$$

$$f_k = s_{ijk}\frac{\partial u_j}{\partial x_i} + \kappa_{kl}u_l + m_{kl}\frac{\partial \varphi}{\partial x_l} + h_k\varphi, \tag{8}$$

$$d_l = e_{ijl}\frac{\partial u_j}{\partial x_i} + m_{kl}u_k - \eta_{kl}\frac{\partial \varphi}{\partial x_k} - a_l\varphi, \tag{9}$$

$$\gamma = g_{ij}\frac{\partial u_j}{\partial x_i} + h_k u_k - a_l\frac{\partial \varphi}{\partial x_l} - \beta\varphi, \tag{10}$$

with $c_{ijkl} = C_{ktiq}A_{lt}A_{jq}$, $s_{ijk} = C_{tqir}A_{jr}\frac{\partial A_{kq}}{\partial x_t}$, $\kappa_{kl} = C_{tqrs}\frac{\partial A_{lq}}{\partial x_t}\frac{\partial A_{ks}}{\partial x_r}$, $e_{ijl} = E_{itl}A_{jt}B$, $m_{kl} = E_{tql}B\frac{\partial A_{kq}}{\partial x_t}$, $g_{ij} = E_{itq}A_{jt}\frac{\partial B}{\partial x_q}$, $h_k = E_{tqr}\frac{\partial A_{kq}}{\partial x_t}\frac{\partial B}{\partial x_r}$, $\eta_{kl} = P_{kl}BB$, $a_l = P_{lj}B\frac{\partial B}{\partial x_j}$, and $\beta = P_{tq}\frac{\partial B}{\partial x_t}\frac{\partial B}{\partial x_q}$. It can be seen from Eqs. (7)–(10) that the transformed piezoelectric materials behave remarkably different compared with conventional piezoelectric materials. Firstly, the body force f_k and the charge density per volume γ arise in the transformed constitutive relations. Further, in addition to the conventional piezoelectric coupling term e_{ijl}, the transformed constitutive relations contain both mechanical and electrical Willis coupling caused by the spatial variation of the displacement and electric potential gauges. Specifically, mechanical Willis coupling described by s_{ijk} in the study refers to the cross-coupling between stress and displacement, as well as between body force and displacement gradient, and electrical Willis coupling described by a_l refers to the cross-coupling between electric displacement and electric potential, as well as between charge density per volume and electric field. Note that, in a moving frame, the displacement should be measured with respect to the moving frame, as the grounded springs κ_{kl} of transformed piezoelectric material are mounted to this moving frame. The mutual coupling also appears in electromechanical coupling terms, where the electric field generates the body force through m_{kl} and the electric potential generates the stress through g_{ij} for actuation, and, meanwhile, the displacement produces the electric displacement through m_{kl} and the displacement gradient produces the volume charge through g_{ij} for sensing. Together, Eqs. (7)–(10) can be regarded as a general constitutive relation of piezoelectricity. Secondly, the transformed piezoelectric materials display polarity. On the one hand, the rigid-body rotation and translation give rise to asymmetric stress, as $c_{ijkl} \neq c_{ijlk} \neq c_{jilk}$ and $s_{ijk} \neq s_{jik}$. This requires a body torque for equilibrium. The polar direction in the study is defined as the direction of the body torque arising in the transformed piezoelectric material, which is along $(\sigma_{ji}-\sigma_{ij})/|\sigma_{ji}-\sigma_{ij}|\epsilon_{ijk}\mathbf{e}_k$. Further, since $e_{ijk} \neq e_{jik}$ and $g_{ij} \neq g_{ji}$, the electric field and electric potential also generate asymmetric stress and body torque in stark contrast to conventional piezoelectric materials where only symmetric stress is generated. On the other hand, due to the combination of polarity and Willis coupling, rigid-body rotation induces not only body force, but electric field, and electric potential (see the first terms in Eqs. (8)–(10)), whereas the piezoelectric materials found so far are free from rigid-body rotation. The combined effects of Willis coupling and polarity have been shown in elasticity [48], but have never been reported in piezoelectricity.

For the purpose of actuation, it is convenient to select a constant electric potential gauge B such that the piezoelectric constitutive relations in Eqs. (7)–(10) can be simplified as

$$\sigma_{ij} = c_{ijkl}\frac{\partial u_l}{\partial x_k} + s_{ijk}u_k + e_{ijl}\frac{\partial \varphi}{\partial x_l}, \tag{11}$$

$$f_k = s_{ijk}\frac{\partial u_j}{\partial x_i} + \kappa_{kl}u_l + m_{kl}\frac{\partial \varphi}{\partial x_l}, \tag{12}$$

$$d_l = e_{ijl}\frac{\partial u_j}{\partial x_i} + m_{kl}u_k - \eta_{kl}\frac{\partial \varphi}{\partial x_k}. \tag{13}$$

Clearly, the charge density per volume and the electric potential disappear in Eqs. (11)–(13), and the mechanical behavior can be controlled by the electric field alone. Note also that, in the equations, the piezoelectric cross-coupling between displacement and electric displacement as well as between electric field and body force sustains. This piezoelectric Willis constitutive relations coincide with the constitutive relations attained from elastodynamic homogenization of piezoelectric composites with asymmetric periodic cells [50–53].

3. Discretization

The continuum piezoelectric gauge transformation offers a clear view of the underlying macroscopic piezoelectric properties needed for the desired actuation, but provides no clues on how to design a lattice displaying the required piezoelectric Willis coupling as well as the polar properties. Instead of applying numerical methods, e.g. topology optimization or data-driven approaches, we consider a simple piezoelectric lattice (e.g. a triangular lattice) in the virtual space and perform piezoelectric gauge transformation over the discrete lattice. Our key hypothesis is that the simple piezoelectric lattice can be equivalent to a continuum material by homogenization. By performing the same piezoelectric gauge transformation over the simple lattice and its equivalent continuum material, the transformed lattice should satisfy the desired piezoelectric properties transformed from the homogenized properties of the continuum material automatically. Thus, we next discretize the continuum piezoelectric gauge transformation by operating the transformation over discrete lattices. To perform this procedure, we consider a virtual discrete lattice composed of an array of linear piezoelectric springs, which can be realized using piezoelectric bars with electrodes mounted on the top and bottom surfaces (see Fig. 2a). The piezoelectric spring is placed between two nodes at $\mathbf{x}^{(i)}$ and $\mathbf{x}^{(j)}$, and the elastic constant, piezoelectric constant, dielectric constant and direction of the piezoelectric spring are denoted as $K_{j,i}$, $E_{j,i}$, $P_{j,i}$ and $\mathbf{N}_{j,i} = \left(\mathbf{x}^{(j)} - \mathbf{x}^{(i)}\right) / \left\|\mathbf{x}^{(j)} - \mathbf{x}^{(i)}\right\|$, respectively. Let $\mathbf{U}^{(i)}$ be the displacement at the node i and $\phi^{(i)}$ the electric potential on the electrode connected to the node i. The constitutive relations of the virtual piezoelectric spring can be written as

$$\mathbf{F}_{j,i} = K_{j,i}\mathbf{N}_{j,i} \otimes \mathbf{N}_{j,i}\left(\mathbf{U}^{(j)} - \mathbf{U}^{(i)}\right) + E_{j,i}\mathbf{N}_{j,i}\left(\phi^{(j)} - \phi^{(i)}\right), \tag{14}$$

$$Q_{j,i} = E_{j,i}\left\langle\left(\mathbf{U}^{(j)} - \mathbf{U}^{(i)}\right), \mathbf{N}_{j,i}\right\rangle + P_{j,i}\left(\phi^{(j)} - \phi^{(i)}\right), \tag{15}$$

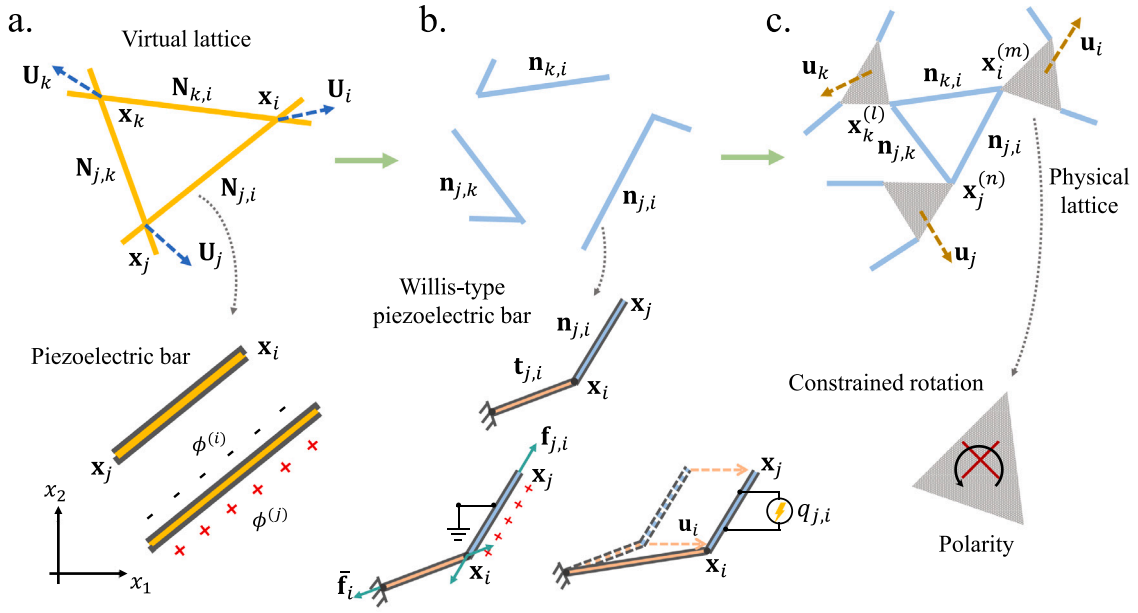

Fig. 2. Schematic representation of discrete piezoelectric gauge transformation for the inverse design of piezoelectric lattices. (a) A virtual lattice consists of an array of piezoelectric springs. The piezoelectric spring can be realized using a piezoelectric bar with electrodes mounted on the top and bottom surfaces. (b) Transformed piezoelectric springs become Willis-type piezoelectric springs with both internal and ground springs and are located in different directions in the physical space. Clearly, they cannot form a well-connected lattice without adjustment. For the Willis-type piezoelectric spring, the voltage applied to the internal spring produces a force on the grounded spring, and the change in length of the grounded spring induces a charge on the internal spring. (c) Transformed piezoelectric lattice after proper geometric adjustment using rigid masses of different shapes. The rotational degrees of freedom of the rigid masses are suppressed, leading to the required polarity.

where $\mathbf{F}_{j,i}$ denotes the spring force applied to the node $\mathbf{x}^{(i)}$ and $Q_{j,i}$ represents the accumulated charge on the electrode connected to the node $\mathbf{x}^{(i)}$. Note that the subscript "j, i" does not denote spatial differentiation.

The potential energy of the virtual piezoelectric spring then reads

$$\mathcal{E}_{j,i} = \frac{1}{2}K_{j,i}\left\langle\left(\mathbf{U}^{(j)}-\mathbf{U}^{(i)}\right),\mathbf{N}_{j,i}\right\rangle^2 + E_{j,i}\left\langle\left(\mathbf{U}^{(j)}-\mathbf{U}^{(i)}\right),\mathbf{N}_{j,i}\right\rangle\left(\phi^{(j)}-\phi^{(i)}\right) + \frac{1}{2}P_{j,i}\left(\phi^{(j)}-\phi^{(i)}\right)^2, \tag{16}$$

where $\langle,\rangle$ represents the dot product.

Similar to the continuum piezoelectric gauge transformation, we introduce the displacement and electric potential gauges for each of the discrete nodes in the lattice, which are defined as $\mathbf{U}^{(i)} = \mathbf{A}_i{}^T\mathbf{u}^{(i)}$ and $\phi^{(i)} = B_i\varphi^{(i)}$, respectively, to achieve the desired displacement $\mathbf{u}^{(i)}$ upon the application of the electric potential $\varphi^{(i)}$. The potential energy of each of the piezoelectric springs remains the same before and after the transformation. Implementing $\mathbf{u}^{(i)}$ and $\varphi^{(i)}$ into Eq. (16), we obtain the formula of the transformed potential energy as

$$\begin{aligned}\varepsilon_{j,i} = \mathcal{E}_{j,i} =& \frac{1}{2}\left[k_{j,i}\left\langle\mathbf{u}_{j,i},\mathbf{n}_{j,i}\right\rangle + \hat{k}_{j,i}\left\langle-\mathbf{u}^{(i)},\mathbf{t}_{j,i}\right\rangle\right]\left\langle\mathbf{u}_{j,i},\mathbf{n}_{j,i}\right\rangle \\ &+ \frac{1}{2}\left[\hat{k}_{j,i}\left\langle\mathbf{u}_{j,i},\mathbf{n}_{j,i}\right\rangle + \widetilde{k}_{j,i}\left\langle-\mathbf{u}^{(i)},\mathbf{t}_{j,i}\right\rangle\right]\left\langle-\mathbf{u}^{(i)},\mathbf{t}_{j,i}\right\rangle \\ &+ \left[e_{j,i}\left\langle\mathbf{u}_{j,i},\mathbf{n}_{j,i}\right\rangle + \hat{e}_{j,i}\left\langle-\mathbf{u}^{(i)},\mathbf{t}_{j,i}\right\rangle\right]\varphi_{j,i} \\ &+ \left[\bar{e}_{j,i}\left\langle\mathbf{u}_{j,i},\mathbf{n}_{j,i}\right\rangle + \widetilde{e}_{j,i}\left\langle-\mathbf{u}^{(i)},\mathbf{t}_{j,i}\right\rangle\right]\left(-\varphi^{(i)}\right) \\ &+ \frac{1}{2}\left[p_{j,i}\varphi_{j,i} - \hat{p}_{j,i}\varphi^{(i)}\right]\varphi_{j,i} + \frac{1}{2}\left[\hat{p}_{j,i}\varphi_{j,i} - \widetilde{p}_{j,i}\varphi^{(i)}\right]\left(-\varphi^{(i)}\right),\end{aligned} \tag{17}$$

where $\mathbf{u}_{j,i} = \mathbf{u}^{(j)} - \mathbf{u}^{(i)}$, $\varphi_{j,i} = \varphi^{(j)} - \varphi^{(i)}$, $\mathbf{n}_{j,i} = \mathbf{A}_j\mathbf{N}_{j,i}/\left\|\mathbf{A}_j\mathbf{N}_{j,i}\right\|$, $\mathbf{t}_{j,i} = \left(\mathbf{A}_i-\mathbf{A}_j\right)\mathbf{N}_{j,i}/\left\|\left(\mathbf{A}_i-\mathbf{A}_j\right)\mathbf{N}_{j,i}\right\|$, $k_{j,i} = K_{j,i}\left\|\mathbf{A}_j\mathbf{N}_{j,i}\right\|^2$, $\hat{k}_{j,i} = K_{j,i}\left\|\mathbf{A}_j\mathbf{N}_{j,i}\right\|\left\|\left(\mathbf{A}_i-\mathbf{A}_j\right)\mathbf{N}_{j,i}\right\|$, $\widetilde{k}_{j,i} = K_{j,i}\left\|\left(\mathbf{A}_i-\mathbf{A}_j\right)\mathbf{N}_{j,i}\right\|^2$, $e_{j,i} = E_{j,i}B_j\left\|\mathbf{A}_j\mathbf{N}_{j,i}\right\|$, $\hat{e}_{j,i} = E_{j,i}B_j\left\|\left(\mathbf{A}_i-\mathbf{A}_j\right)\mathbf{N}_{j,i}\right\|$, $\bar{e}_{j,i} = E_{j,i}\left(B_i-B_j\right)\left\|\mathbf{A}_j\mathbf{N}_{j,i}\right\|$, $\widetilde{e}_{j,i} = E_{j,i}\left(B_i-B_j\right)\left\|\left(\mathbf{A}_i-\mathbf{A}_j\right)\mathbf{N}_{j,i}\right\|$, $p_{j,i} = P_{j,i}B_jB_j$, $\hat{p}_{j,i} = P_{j,i}B_j\left(B_i-B_j\right)$, and $\widetilde{p}_{j,i} = P_{j,i}\left(B_i-B_j\right)^2$. By taking derivatives of the transformed potential energy (Eq. (17)) with respect to $\mathbf{u}_{j,i}$, $\mathbf{u}^{(i)}$, $\varphi_{j,i}$, and $\varphi^{(i)}$, we attain the internal spring force, the grounded spring force (functioned as the body force), the free charge from the internal spring, and the free charge from the grounded spring, respectively, as

$$\mathbf{f}_{j,i} = k_{j,i}\mathbf{n}_{j,i}\otimes\mathbf{n}_{j,i}\mathbf{u}_{j,i} - \hat{k}_{j,i}\mathbf{n}_{j,i}\otimes\mathbf{t}_{j,i}\mathbf{u}^{(i)} + e_{j,i}\mathbf{n}_{j,i}\varphi_{j,i} - \bar{e}_{j,i}\mathbf{n}_{j,i}\varphi^{(i)}, \tag{18}$$

$$\bar{\mathbf{f}}_i = \hat{k}_{j,i}\mathbf{t}_{j,i}\otimes\mathbf{n}_{j,i}\mathbf{u}_{j,i} - \widetilde{k}_{j,i}\mathbf{t}_{j,i}\otimes\mathbf{t}_{j,i}\mathbf{u}^{(i)} + \hat{e}_{j,i}\mathbf{t}_{j,i}\varphi_{j,i} - \widetilde{e}_{j,i}\mathbf{t}_{j,i}\varphi^{(i)}, \tag{19}$$

$$q_{j,i} = e_{j,i}\left\langle\mathbf{u}_{j,i},\mathbf{n}_{j,i}\right\rangle - \hat{e}_{j,i}\left\langle\mathbf{u}^{(i)},\mathbf{t}_{j,i}\right\rangle + p_{j,i}\varphi_{j,i} - \hat{p}_{j,i}\varphi^{(i)}, \tag{20}$$

$$q_i = \bar{e}_{j,i}\left\langle\mathbf{u}_{j,i},\mathbf{n}_{j,i}\right\rangle - \widetilde{e}_{j,i}\left\langle\mathbf{u}^{(i)},\mathbf{t}_{j,i}\right\rangle + \hat{p}_{j,i}\varphi_{j,i} - \widetilde{p}_{j,i}\varphi^{(i)}. \tag{21}$$

Clearly, a conventional piezoelectric spring in the virtual lattice is transformed to two nonstandard piezoelectric springs coupled with each other in the physical lattice (see Fig. 2b): One is the internal piezoelectric spring with a new set of elastic constant $k_{j,i}$, piezoelectric constant $e_{j,i}$, and dielectric constant $p_{j,i}$ and along the direction of $\mathbf{n}_{j,i}$; The other is the grounded piezoelectric spring with elastic constant $\widetilde{k}_{j,i}$, piezoelectric constant $\widetilde{e}_{j,i}$ and dielectric constant $\widetilde{p}_{j,i}$ and along the direction of $\mathbf{t}_{j,i}$. Note that the top and bottom electrodes of the internal piezoelectric spring are applied with the electric potential $\varphi^{(i)}$ and $\varphi^{(j)}$, respectively, while the top electrode of the grounded piezoelectric spring is applied with the electric potential $\varphi^{(i)}$ and the bottom electrode of the grounded piezoelectric spring is electrically grounded. Remarkably, cross-coupling between the two piezoelectric springs is observed in both mechanical and electrical domains, which we call mechanical and electrical Willis coupling, respectively. In particular, $\hat{k}_{j,i}$ describes the mechanical Willis coupling, where the change in length of the grounded spring produces a force on the internal spring and vice versa. On the other hand, $\hat{p}_{j,i}$ describes the electrical Willis coupling, where the change in the electric potential of the grounded spring produces a charge in the internal spring and vice versa. In addition to these two types of Willis coupling, piezoelectric responses of the two springs are also coupled, e.g. the electric potential applied on the grounded spring also generates a force in the internal spring through the term $\bar{e}_{j,i}$, and the electric voltage applied on the internal spring induces a force on the grounded spring through the term $\hat{e}_{j,i}$ (see the lower panel in Fig. 2b). Similar properties of the Willis coupling

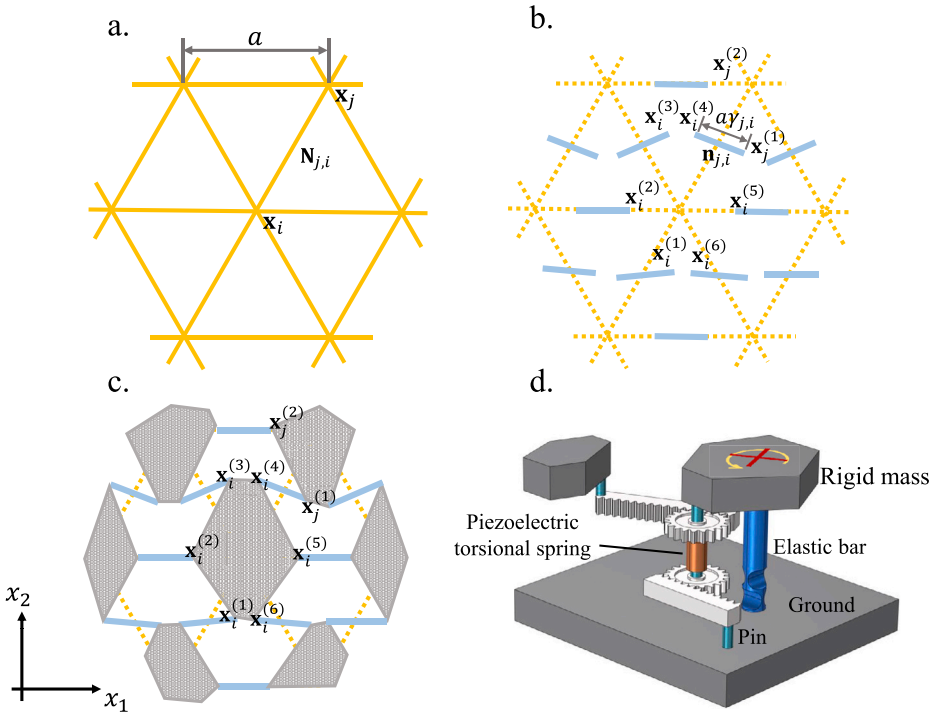

Fig. 3. Design procedures of the transformed piezoelectric lattice. (a) A triangle lattice composed of linear piezoelectric springs with the free length a in the virtual space. (b) The spatial arrangement of the transformed piezoelectric springs in the physical space, where only internal springs are shown. (c) Rigid masses are properly added between the transformed internal piezoelectric springs. (d) A possible ready-to-fabricate metamaterial structure for the realization of the required piezoelectric Willis spring.

also exist in Eqs. (20) and (21), where deformation of the grounded spring induces a charge in the internal spring based on $\widehat{e}_{j,i}$ and vice versa based on $\overline{e}_{j,i}$. Note also that the transformed internal spring is no longer along the direction of its virtual spring as $\mathbf{n}_{j,i} \neq \mathbf{N}_{j,i}$. Consequently, internal springs cannot be properly connected following the geometric setup of the virtual lattice (see the upper panel in Fig. 2b). To ensure proper connections of the transformed piezoelectric springs, we turn point masses in the virtual lattice into rigid-body masses in the physical lattice (see Fig. 2c). Since rotational degrees of freedom of point masses vanish in the virtual lattice, rotations of the rigid-body masses in the physical lattice should be suppressed, giving rise to polarity. In summary, the desired piezoelectric responses can be realized when the physical lattice satisfies Eqs. (18)–(21) as well as the polarity. Piezoelectric Willis coupling and polarity found in the physical lattice coincide with those of the continuum piezoelectric gauge transformation.

To simplify the control and operation of the transformed piezoelectric lattice, we implement a constant electric potential gauge among all nodes of the lattice ($B_i = B_j$). Further, we ground one of the two electrodes on the internal piezoelectric spring ($\varphi^{(i)} = 0$), and connect all the other electrodes within the lattice ($\varphi^{(j)} = \varphi$). In doing so, we aim to achieve the desired displacement field $\mathbf{u}^{(i)}$ by applying the electric potential φ throughout the lattice. With these assumptions, the constitutive relations of the transformed piezoelectric springs are reduced to

$$\mathbf{f}_{j,i} = k_{j,i}\mathbf{n}_{j,i} \otimes \mathbf{n}_{j,i}\mathbf{u}_{j,i} - \widehat{k}_{j,i}\mathbf{n}_{j,i} \otimes \mathbf{t}_{j,i}\mathbf{u}^{(i)} + e_{j,i}\mathbf{n}_{j,i}\varphi, \tag{22}$$

$$\bar{\mathbf{f}}_i = \widehat{k}_{j,i}\mathbf{t}_{j,i} \otimes \mathbf{n}_{j,i}\mathbf{u}_{j,i} - \widetilde{k}_{j,i}\mathbf{t}_{j,i} \otimes \mathbf{t}_{j,i}\mathbf{u}^{(i)} + \widehat{e}_{j,i}\mathbf{t}_{j,i}\varphi, \tag{23}$$

$$q_{j,i} = e_{j,i}\left\langle \mathbf{u}_{j,i}, \mathbf{n}_{j,i} \right\rangle - \widehat{e}_{j,i}\left\langle \mathbf{u}^{(i)}, \mathbf{t}_{j,i} \right\rangle + p_{j,i}\varphi. \tag{24}$$

It can be seen that the free charge appears on the internal spring, but is absent on the grounded spring ($q_i = 0$). Further, besides the mechanical Willis coupling $\widehat{k}_{j,i}$, one set of non-standard piezoelectric Willis coupling $\widehat{e}_{j,i}$ remains in the transformed springs. As a result, the voltage applied on the internal spring produces a force on the grounded spring. At the same time, the change in length of the grounded spring induces a charge on the internal spring. The reduced equations of the discrete lattice (Eqs. (22)–(24)) display the same properties as those in Eqs. (11)–(13). However, realization of the nonstandard piezoelectric properties shown in Eqs. (22)–(24) using discrete lattices presents challenges. This type of design has never been attempted.

4. Lattice construction

In this section, we suggest a design guideline to physically construct the transformed piezoelectric lattice. First, our attention is focused on the spatial arrangement of the interconnected internal springs and rigid masses. As an illustrative example, we select a triangular lattice in the virtual space (see Fig. 3a), where the point masses are placed at the node $\mathbf{x}_i$ and the linear piezoelectric springs with the length a are located between $\mathbf{x}_i$ and $\mathbf{x}_j$. We enforce the center of the virtual and transformed internal springs remaining in the same position $\frac{\mathbf{x}_i+\mathbf{x}_j}{2}$, but changing the length of the transformed spring to $a\gamma_{j,i}$ with $0 < \gamma_{j,i} < 1$ for proper connections. Calculating the direction of each of the internal springs $\mathbf{n}_{j,i}$, the positions of all the internal springs are determined as the blue lines shown in Fig. 3b. We assign one of the two nodes of each of the internal springs adjacent to the virtual node $\mathbf{x}_i$ as the new node (e.g. $\mathbf{x}_i^{(j)}$, $j = 1, 2, 3, \ldots, 6$) to build a rigid polygon mass connecting all the transformed internal springs that are originally connected at $\mathbf{x}_i$ in the virtual lattice (see Fig. 3c). Duplicating this procedure among the nodes in the virtual lattice, the spatial arrangement and geometry of the internal springs and rigid masses of the transformed piezoelectric lattice are determined.

Next, we propose a physically realizable design to achieve the required piezoelectric Willis coupling dictated in Eqs. (22)–(24). For this purpose, a gear system incorporated with a piezoelectric torsional spring is employed (see Fig. 3d). In particular, the gear system consists of two pairs of rack-and-pinion-gear structures. One pair of the gear structures connects the rigid mass with its adjacent rigid mass along the

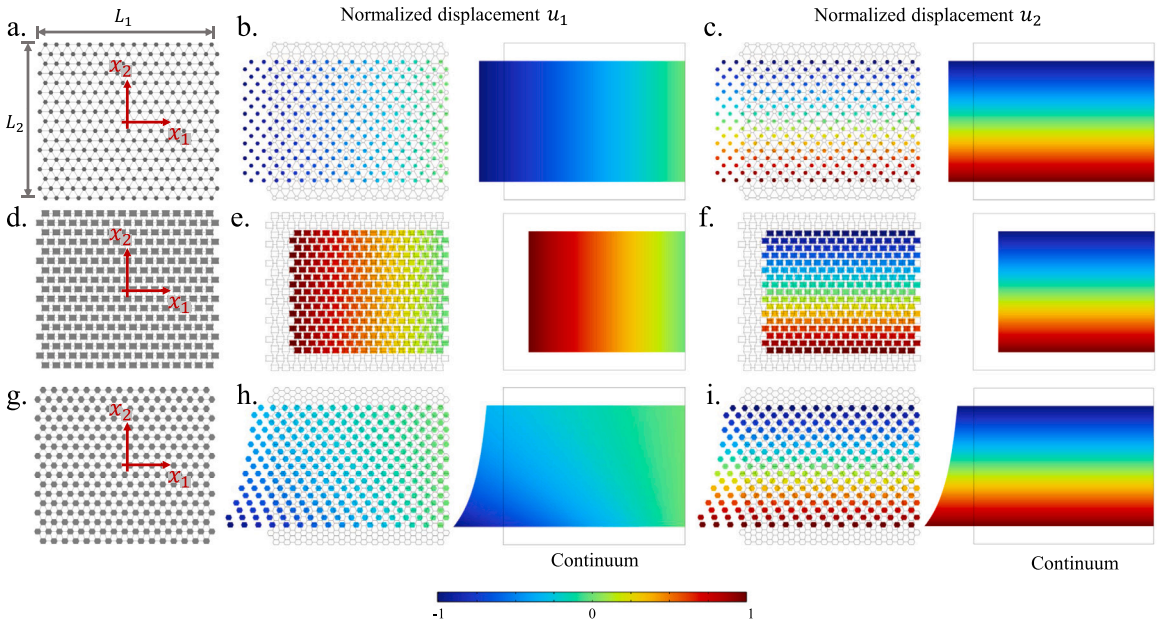

Fig. 4. Geometry and numerical simulations of the piezoelectric lattices before and after the transformation. (a) Geometry of a triangular piezoelectric lattice before the transformation. (b, c) Simulated displacement fields of the triangular piezoelectric lattice actuated by an electric voltage. Left panel: discrete lattice; Right panel: Continuum material. (b) Displacement u_1; (c) Displacement u_2. (d, g) Geometry of two transformed piezoelectric lattices. (e, f, h, i) Simulated displacement fields of the transformed piezoelectric lattices actuated by an electric voltage. Left panel: discrete lattice; Right panel: Continuum material. (e, h) Displacement u_1; (f, i) Displacement u_2. The displacement gauge $A_{11} = -1$ in (d–f), $A_{11} = x_2/L_2 + 1$ in (g–i).

direction of the internal spring. The other pair of the gear structures connects the rigid mass to the reference ground along the direction of the grounded spring. A piezoelectric torsional spring composed of a piezoelectric hollow cylinder operating in shear mode is installed between the two gears. This simple design can realize the required mechanical and piezoelectric Willis coupling automatically. For example, when the distance between the two rigid masses changes, a force is generated in the rack connected to the ground due to the deformation of the rotational spring. Similarly, when the rigid mass moves, a force is induced in the rack connected between the two rigid masses, giving rise to the mechanical Willis coupling. Further, when a voltage is applied on the piezoelectric torsional spring, two torques are generated on the two gears, leading to two forces in the internal and grounded springs as required by the piezoelectric Willis coupling. Finally, to suppress rotations of rigid masses, an elastic bar with two indentations is introduced between each of the rigid masses and the reference ground (see Fig. 3d). Replacing each of the internal springs shown in Fig. 3c with the designed gear system results in fabricable architected transducers with desired piezoelectric responses.

To validate the design, numerical simulations are performed for transformed piezoelectric lattices obtained using presumed displacement and electric potential gauges. A commercial finite element software, COMSOL Multiphysics, is employed for the simulation, where two-dimensional plane stress assumptions are applied for simplicity. We build transformed piezoelectric lattices containing 15×16 unit cells according to the approach introduced in Fig. 3b, where $a = 10$ mm and $\gamma_{j,i} = 0.4$. The internal and grounded piezoelectric springs are modeled using equivalent point forces applied on rigid masses described following Eqs. (22)–(24), where $K_{j,i} = 5.8 \times 10^7$ N/m, $E_{j,i} = 6.62$ C/m, and $P_{j,i} = 1704$ F. In simulations, the rigid masses are modeled by elastic bodies, but with a modulus large enough to ignore their deformation. The horizontal displacement of the right boundary is zero ($u_1(x_1 = \frac{L_1}{2}) = 0$), and the center on the right boundary is fixed ($u_1(x_1 = \frac{L_1}{2}, x_2 = 0) = 0$, $u_2(x_1 = \frac{L_1}{2}, x_2 = 0) = 0$). All other boundaries are free. In this way, the piezoelectric lattice metamaterial is allowed to elongate or contract along both x_1 and x_2 directions, while eliminating rigid-body translations and rotations. Fig. 4 shows the lattice structures and their displacement fields u_1 and u_2 from simulations when an electric voltage is applied. For comparison, Figs. 4a–4c show the results of the triangular lattice before transformation. In Figs. 4b and 4c, we also calculate the displacement fields of the continuum piezoelectric material for validation. The effective continuum piezoelectric material parameters of the lattice are attained using a homogenization approach [48]. We calculate the homogenized bulk modulus $\lambda = 25$ MPa, shear modulus $\mu = 25$ MPa, piezoelectric coefficients $E_{113} = -46.3$ C/m^2, $E_{333} = 139.0$ C/m^2 (others are zero), and dielectric constants $P_{11} = P_{33} = 8.7\times10^5$ F/m (others are zero). The triangular lattice is isotropic and homogeneous. Thus, it can be seen from Figs. 4b and 4c that the lattice elongates uniformly along the x_1 direction and contracts uniformly along the x_2 direction when applied with an electric voltage. This behavior is similar to that of standard piezoelectric materials. The results of the discrete lattice and continuum material are in excellent agreement.

Next, we implement a displacement gauge in the form of $\mathbf{A}^T = \begin{bmatrix} A_{11}(x_1, x_2) & 0 \\ 0 & 1 \end{bmatrix}$ to modulate the displacement u_1 while keep the displacement u_2 unchanged and let the electric potential gauge $B = 1$ (see Figs. 4d–4i). In the first example, we select $A_{11} = -1$ so that the elongation along the x_1 direction before transformation becomes contraction after transformation (see Fig. 4e). Yet, the displacement u_2 remains the same contraction before and after the transformation (see Fig. 4f). Thus, the piezoelectric lattice shown in Fig. 4d displays a negative Poisson's ratio. Note that both the mechanical and piezoelectric Willis coupling coefficients $\hat{k}_{j,i}$ and $\hat{e}_{j,i}$ are zero in this case, since the displacement gauge is constant in space. Consequently, the negative Poisson's ratio is caused by the geometry and polarity of the piezoelectric lattice. It can be easily checked that the geometry of the lattice is similar to auxetic lattices developed in other studies [54–56]. In Fig. 4g, we select $A_{11} = x_2/L_2 + 1$ to produce a deformation profile varied with x_2. As expected, the upper part of the piezoelectric lattice is compressed and the lower part is extended once the voltage is applied (see Figs. 4h and 4i). To realized this non-uniform deformation, both the mechanical and piezoelectric Willis coupling coefficients $\hat{k}_{j,i}$ and $\hat{e}_{j,i}$ must be nonzero, such that the piezoelectric lattice should be connected

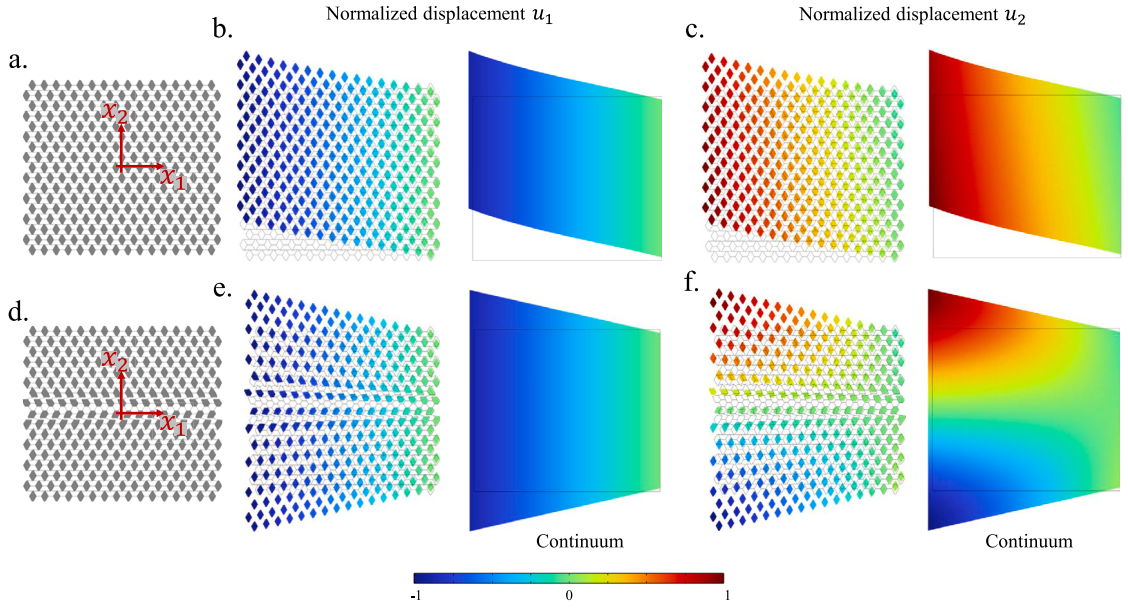

Fig. 5. Geometry and numerical simulations of the transformed piezoelectric lattices. (a, d) Geometry of two transformed piezoelectric lattices. (b, c, e, f) Simulated displacement fields of the transformed piezoelectric lattices actuated by an electric voltage. Left panel: discrete lattice; Right panel: Continuum material. (b, e) Displacement u_1; (c, f) Displacement u_2. The displacement gauge $A_{12} = 10\cosh(x_1/L_1)$ in (a–c), $A_{12} = 10\sin(\pi x_2/L_2)$ in (d–f).

to the ground. Consequently, the desired displacement field is caused by the combined effects of material heterogeneity and ground connections. This type of non-uniform deformation is difficult to be excited in conventional piezoelectric materials, as they are homogeneous and free-standing.

In Fig. 5, we change the form of the displacement gauge to $\mathbf{A}^T = \begin{bmatrix} 1 & 0 \\ A_{12}(x_1, x_2) & 1 \end{bmatrix}$ to modulate the displacement u_2 in function of u_1, while keeping u_1 unchanged. In Figs. 5a–5c, $A_{12} = 10\cosh(x_1/L_1)$ and $u_2 = U_2 - A_{12}U_1$ so that the piezoelectric lattice undergoes simple shear along the x_2 direction when the voltage is applied. Note that, for the simple deformation, u_2 is not a linear function of x_1. On the other hand, in Figs. 5d–5f, $A_{12} = 10\sin(\pi x_2/L_2)$ so that most of the left-hand side portion of the piezoelectric lattice elongates along the vertical direction but the portion near the right-hand side boundary contracts due to the Poisson's effect when the voltage is applied. However, the displacement u_1 remains unchanged after the transformation for all the cased in Fig. 5. Overall, in Figs. 4 and 5, excellent agreement in displacement fields between the transformed piezoelectric lattices and their continuum counterpart is observed, which also coincides with the expected displacement fields calculated analytically using the displacement gauge. The results shown in Figs. 4 and 5 verify the validity of the theory and the design.

5. Inverse design

In this section, we show how the piezoelectric gauge transformation and its related material construction guidelines demonstrated in previous sections enable the inverse design of architected piezoelectric actuators. We focus on two illustrative examples for this purpose. The first example is the inverse design of piezoelectric lattices to achieve a desired shape with the application of a voltage, and the second example explores the possibility of achieving a desired strain field. Note that the applied voltages among all piezoelectric springs in the designed lattice are the same. During the inverse design, the first step is to determine the displacement field after the transformation. In the first example, our goal is to deform a rectangular piezoelectric lattice to a circle upon the application of a voltage. To achieve this, we propose a mapping scheme for the positions of the discrete nodes before and after the deformation: $x_1' = \frac{x_1}{c_1}\sqrt{1 - \frac{x_2^2}{2r^2c_2^2}}$ and $x_2' = \frac{x_2}{c_2}\sqrt{1 - \frac{x_1^2}{2r^2c_1^2}}$ (see Fig. 6), where x_1' and x_2' are the positions of the nodes after the deformation, and $c_1 = \frac{L_1}{2r}, c_2 = \frac{L_2}{2r}$ with r being the radius of the deformed circle. As a result, the transformed displacement can be determined as $u_1(x_1, x_2) = x_1' - x_1 = \frac{x_1}{c_1}\left(\sqrt{1 - \frac{x_2^2}{2r^2c_2^2}} - c_1\right)$ and $u_2(x_1, x_2) = x_2' - x_2 = \frac{x_2}{c_2}\left(\sqrt{1 - \frac{x_1^2}{2r^2c_1^2}} - c_2\right)$.

In the second step, the displacement gauge $\mathbf{A}^T$ is identified based on the displacement field of the virtual lattice and the desire displacement field of the transformed lattice. It is worth mentioning that since the displacement gauge matrix is invertible, zero displacement in transformed lattice should be avoided. Further, the displacement gauge matrix contains four entities in 2D. However, only two equations can be attained from the relationships between the displacement fields before and after the transformation. To ensure unique solutions of the displacement gauge matrix, we enforce two of the entities in the displacement gauge matrix as known constants. Consequently, four types of designs are possible: Design I for $\mathbf{A}^T = \begin{bmatrix} A_{11} & 0 \\ 0 & A_{22} \end{bmatrix}$; Design II for $\mathbf{A}^T = \begin{bmatrix} A_{11} & 0 \\ A_{12} & 1 \end{bmatrix}$; Design III for $\mathbf{A}^T = \begin{bmatrix} 1 & A_{21} \\ 0 & A_{22} \end{bmatrix}$; and Design IV for $\mathbf{A}^T = \begin{bmatrix} 1 & A_{21} \\ A_{12} & 1 \end{bmatrix}$. In the last step, the four transformed lattices are created following the discrete piezoelectric gauge transformation and lattice construction guidelines (see Fig. 7). Numerical simulations are performed to validate the desired shape change excited by the applied voltage for the four designs shown in Fig. 7, where the required circular shapes of deformation are clearly seen. In the simulations, the point in the center of the piezoelectric metamaterial is fixed ($u_1(x_1 = 0, x_2 = 0) = 0$, $u_2(x_1 = 0, x_2 = 0) = 0$), and the horizontal displacement of the center on the upper boundary is zero ($u_1(x_1 = 0, x_2 = \frac{L_2}{2}) = 0$). All other boundaries are free. Consequently, the piezoelectric lattice metamaterial can deform freely without rigid-body translations and rotations.

In the second example, our aim is to achieve the desired strain field by applying a voltage on the designed piezoelectric lattice. We assign two normal distribution functions on the two desired normal strains as

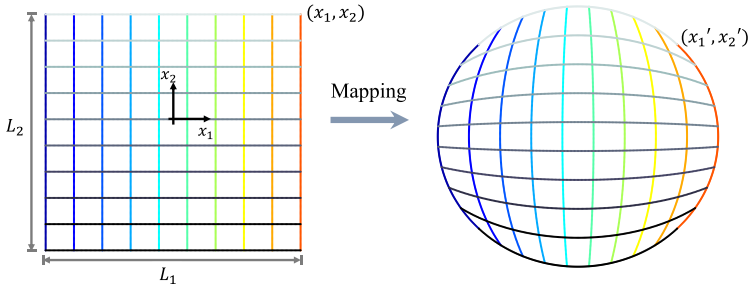

Fig. 6. Schematic of a geometric mapping from a rectangle to a circle.

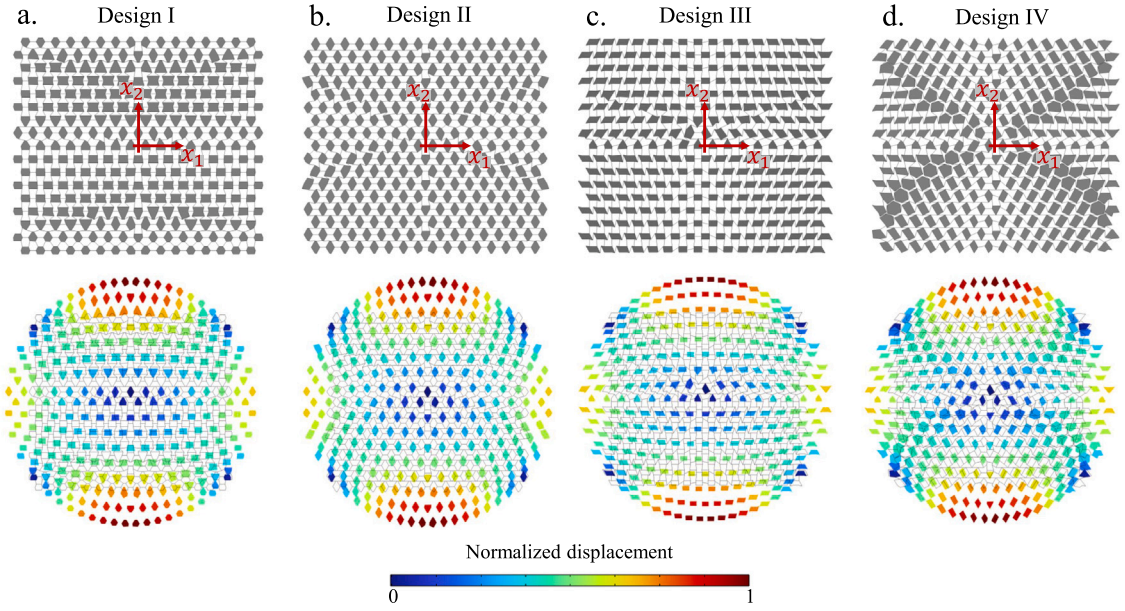

Fig. 7. Geometry and numerical simulations of the transformed piezoelectric lattices for desired shape changes. Top row: Geometry; Bottom row: Simulated total displacement fields. (a) Design I; (b) Design II; (c) Design III; (d) Design IV.

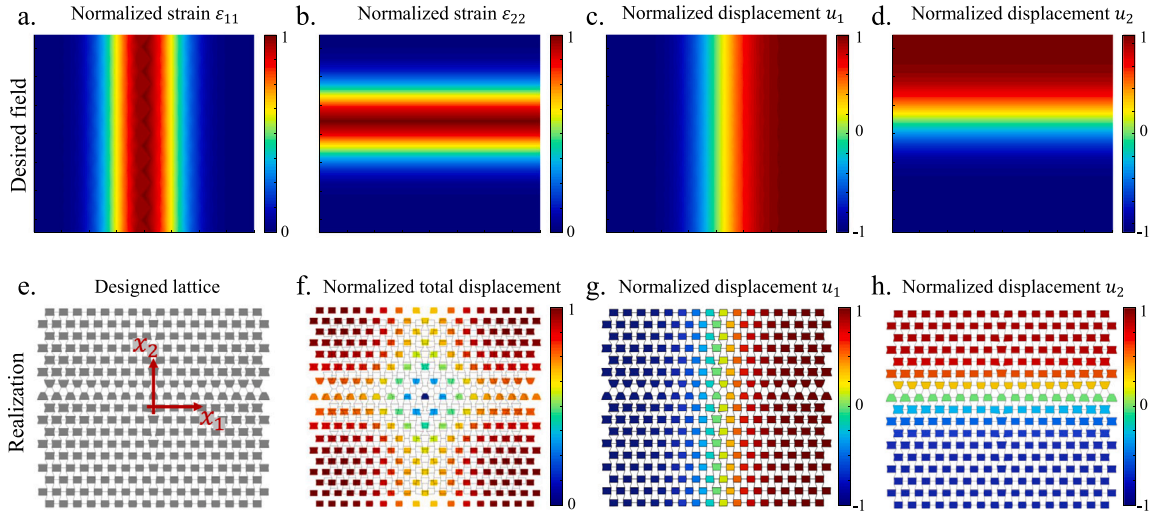

Fig. 8. Inverse design of a piezoelectric lattice to achieve a desired strain field under a given voltage. (a–d) Desired strain and the corresponding displacement fields. (a) Normal strain ε_{11}; (b) Normal strain ε_{22}; (c) Displacement u_1; (d) Displacement u_2. (e) Geometry of the designed piezoelectric lattice. (f–h) Simulated displacement fields of the piezoelectric lattice applied with an electric voltage. (f) Total displacement field; (g) Displacement u_1; (h) Displacement u_2.

$\varepsilon_{11} = \frac{1}{\sqrt{2\pi}} e^{\frac{-(\hat{c}_1 x_1/L_1)^2}{2}}$ and $\varepsilon_{22} = \frac{1}{\sqrt{2\pi}} e^{\frac{-(\hat{c}_2 x_2/L_2)^2}{2}}$, where $\hat{c}_1 = \hat{c}_2 = 4$ (see the strain fields in Figs. 8a and 8b). The shear strain is enforced zero, satisfying the strain compatibility conditions. The desired displacement fields are then obtained by calculating the integral of the strain fields. In the calculations, we implement the same displacement boundary

conditions as those in Fig. 7. The desired displacement fields u_1 and u_2 are shown in Figs. 8c and 8d, respectively. It can be seen that u_1 is nearly constant in the left and right portions of the lattice, and u_2 is nearly invariant on the top and bottom portions. We employ Design I to attain the structure of the transformed lattice shown in Fig. 8e. Numerical simulations are performed to validate the design of the transform lattice. Figs. 8f–8h show the total displacement, the displacement u_1 and u_2 when the voltage is applied on the piezoelectric lattice. Excellent agreement is clearly seen between the desired and simulated displacement fields. Finally, it may need to mention that the piezoelectric metamaterials designed can be realized using pin-connected rods [57], or by embedding fabric materials into the connections between thin beams and large rigid-body masses [58] to improve fracture and fatigue resistance.

6. Conclusion

In summary, we develop continuum and discrete piezoelectric gauge transformations for the inverse design of architected piezoelectric transducers to achieve an arbitrary desired displacement field with the application of an electric voltage. We critically analyze the physical principles of the piezoelectric polarity and Willis coupling required by the transformation. According to the discrete transformation, a lattice design guideline is proposed for the construction of the transformed piezoelectric springs. We also suggest a ready-to-fabricate design to realize the piezoelectric polar Willis springs using metamaterial structures. The piezoelectric gauge transformation is validated through a range of numerical simulations. Some nonstandard and appealing displacement control functions due to piezoelectric actuation are demonstrated numerically. Detailed inverse design procedures for achieving the desired shape changes and strain-field control are shown in the last section. The fast analytical inverse design approach can benefit the development of advanced actuators used in ultrasonics, robotics, and other piezoelectric devices. The inverse design strategy enabled by piezoelectric gauge transformation is readily to be extended to other types of responsive materials, e.g. flexoelectric materials where the strain gradient can be flexibly controlled by designing microstructures when the electric polarization is present.

CRediT authorship contribution statement

Li Huang: Writing – original draft, Investigation, Formal analysis, Data curation. **Rui Zhu:** Writing – review & editing, Project administration, Funding acquisition, Formal analysis. **Gengkai Hu:** Writing – review & editing, Formal analysis. **Yangyang Chen:** Writing – review & editing, Writing – original draft, Supervision, Project administration, Methodology, Investigation, Funding acquisition, Formal analysis, Conceptualization.

Declaration of competing interest

The authors declare the following financial interests/personal relationships which may be considered as potential competing interests: Yangyang Chen reports financial support was provided by Hong Kong Research Grants Council. Rui Zhu reports financial support was provided by National Key R&D Program of China. If there are other authors, they declare that they have no known competing financial interests or personal relationships that could have appeared to influence the work reported in this paper.

Acknowledgments

Y.C. acknowledges the support from the Hong Kong Research Grants Council (Grant No. RGC-ECS 26200422). R.Z. acknowledges the support from the National Key R&D Program of China (Grant No. 2021YFE0110900).

Data availability

Data will be made available on request.

References

[1] Oscar Bryan Wilson, An Introduction to the Theory and Design of Sonar Transducers, Naval Sea Systems Command, 1985.
[2] James F. Tressler, Piezoelectric transducer designs for sonar applications, in: Piezoelectric and Acoustic Materials for Transducer Applications, Springer, 2008, pp. 217–239.
[3] Gustav Gautschi, Piezoelectric Sensors, Springer, 2002.
[4] Eli J. Curry, Kai Ke, Meysam T. Chorsi, Kinga S. Wrobel, Albert N. Miller, III, Avi Patel, Insoo Kim, Jianlin Feng, Lixia Yue, Qian Wu, et al., Biodegradable piezoelectric force sensor, Proc. Natl. Acad. Sci. 115 (5) (2018) 909–914.
[5] Kenji Uchino, Piezoelectric Actuators and Ultrasonic Motors, vol. 1, Springer Science & Business Media, 1996.
[6] Brett Watson, James Friend, Leslie Yeo, Piezoelectric ultrasonic micro/milli-scale actuators, Sensors Actuators A: Phys. 152 (2) (2009) 219–233.
[7] Faizan Ali, Waseem Raza, Xilin Li, Hajera Gul, Ki-Hyun Kim, Piezoelectric energy harvesters for biomedical applications, Nano Energy 57 (2019) 879–902.
[8] Nurettin Sezer, Muammer Koç, A comprehensive review on the state-of-the-art of piezoelectric energy harvesting, Nano Energy 80 (2021) 105567.
[9] Jonathan M. Rothberg, Tyler S. Ralston, Alex G. Rothberg, John Martin, Jaime S. Zahorian, Susan A. Alie, Nevada J. Sanchez, Kailiang Chen, Chao Chen, Karl Thiele, et al., Ultrasound-on-chip platform for medical imaging, analysis, and collective intelligence, Proc. Natl. Acad. Sci. 118 (27) (2021) e2019339118.
[10] K. Kirk Shung, J.M. Cannata, Q.F. Zhou, Piezoelectric materials for high frequency medical imaging applications: A review, J. Electroceramics 19 (2007) 141–147.
[11] Junqiu Liu, Hao Tian, Erwan Lucas, Arslan S. Raja, Grigory Lihachev, Rui Ning Wang, Jijun He, Tianyi Liu, Miles H. Anderson, Wenle Weng, et al., Monolithic piezoelectric control of soliton microcombs, Nature 583 (7816) (2020) 385–390.
[12] Diego Emilio Serrano, Roozbeh Tabrizian, Farrokh Ayazi, Tunable piezoelectric MEMS resonators for real-time clock, in: 2011 Joint Conference of the IEEE International Frequency Control and the European Frequency and Time Forum (FCS) Proceedings, IEEE, 2011, pp. 1–4.
[13] Masahiro Shimizu, Chihiro Okamoto, Kenichi Umeda, Shinji Watanabe, Toshio Ando, Noriyuki Kodera, An ultrafast piezoelectric Z-scanner with a resonance frequency above 1.1 MHz for high-speed atomic force microscopy, Rev. Sci. Instrum. 93 (1) (2022).
[14] Ke Bian, Christoph Gerber, Andreas J. Heinrich, Daniel J. Müller, Simon Scheuring, Ying Jiang, Scanning probe microscopy, Nat. Rev. Methods Prim. 1 (1) (2021) 36.
[15] Yongling Wu, Yulin Ma, Hongyu Zheng, Seeram Ramakrishna, Piezoelectric materials for flexible and wearable electronics: A review, Mater. Des. 211 (2021) 110164.
[16] Rumin Fu, Lingjie Tu, Youjun Guan, Zhengao Wang, Chunlin Deng, Peng Yu, Guoxin Tan, Chengyun Ning, Lei Zhou, Intrinsically piezoelectric elastomer based on crosslinked polyacrylonitrile for soft electronics, Nano Energy 103 (2022) 107784.
[17] Aniket Pal, Vanessa Restrepo, Debkalpa Goswami, Ramses V Martinez, Exploiting mechanical instabilities in soft robotics: control, sensing, and actuation, Adv. Mater. 33 (19) (2021) 2006939.
[18] Haojian Lu, Ying Hong, Yuanyuan Yang, Zhengbao Yang, Yajing Shen, Battery-less soft millirobot that can move, sense, and communicate remotely by coupling the magnetic and piezoelectric effects, Adv. Sci. 7 (13) (2020) 2000069.
[19] Xiaohui Yan, Gang Li, Zheyan Wang, Zhichao Yu, Kaiying Wang, Yucheng Wu, Recent progress on piezoelectric materials for renewable energy conversion, Nano Energy 77 (2020) 105180.
[20] Xianfen Chen, Qingtao Zhu, Bei Jiang, Duoduo Li, Xinyi Song, Lijun Huang, Yuanqiao Zhang, Jiabin Chen, Quanping Yuan, Research progress of wood and lignocellulose in sustainable piezoelectric systems, Nano Energy (2024) 109650.
[21] Hongjie Hu, Hao Huang, Mohan Li, Xiaoxiang Gao, Lu Yin, Ruixiang Qi, Ray S. Wu, Xiangjun Chen, Yuxiang Ma, Keren Shi, et al., A wearable cardiac ultrasound imager, Nature 613 (7945) (2023) 667–675.
[22] Muyang Lin, Ziyang Zhang, Xiaoxiang Gao, Yizhou Bian, Ray S. Wu, Geonho Park, Zhiyuan Lou, Zhuorui Zhang, Xiangchen Xu, Xiangjun Chen, et al., A fully integrated wearable ultrasound system to monitor deep tissues in moving subjects, Nature Biotechnol. 42 (3) (2024) 448–457.
[23] Lin Zhang, Colin Marcus, Dabin Lin, David Mejorado, Scott Joseph Schoen, Jr., Theodore T. Pierce, Viksit Kumar, Sara V. Fernandez, David Hunt, Qian Li, et al., A conformable phased-array ultrasound patch for bladder volume monitoring, Nat. Electron. 7 (1) (2024) 77–90.
[24] Wenya Du, Lin Zhang, Emma Suh, Dabin Lin, Colin Marcus, Lara Ozkan, Avani Ahuja, Sara Fernandez, Ikra Iftekhar Shuvo, David Sadat, et al., Conformable ultrasound breast patch for deep tissue scanning and imaging, Sci. Adv. 9 (30) (2023) eadh5325.

[25] Liang Chen, Hui Liu, He Qi, Jun Chen, High-electromechanical performance for high-power piezoelectric applications: Fundamental, progress, and perspective, Prog. Mater. Sci. 127 (2022) 100944.
[26] S.K. Nag, D.C. Agrawal, Piezoelectric and mechanical properties of ceria-doped lead zirconate titanate ceramics, J. Mater. Sci. 27 (1992) 4125–4130.
[27] Sukriti Manna, Geoff L. Brennecka, Vladan Stevanović, Cristian V. Ciobanu, Tuning the piezoelectric and mechanical properties of the AlN system via alloying with YN and BN, J. Appl. Phys. 122 (10) (2017).
[28] Cheng Chen, Xi Wang, Yan Wang, Dandan Yang, Fangyi Yao, Wenxiong Zhang, Bo Wang, Galhenage Asha Sewvandi, Desuo Yang, Dengwei Hu, Additive manufacturing of piezoelectric materials, Adv. Funct. Mater. 30 (52) (2020) 2005141.
[29] Yaokun Pang, Yunteng Cao, Yihang Chu, Minghong Liu, Kent Snyder, Devin MacKenzie, Changyong Cao, Additive manufacturing of batteries, Adv. Funct. Mater. 30 (1) (2020) 1906244.
[30] Sampada Bodkhe, Gabrielle Turcot, Frederick P. Gosselin, Daniel Therriault, One-step solvent evaporation-assisted 3D printing of piezoelectric PVDF nanocomposite structures, ACS Appl. Mater. Interfaces 9 (24) (2017) 20833–20842.
[31] Huachen Cui, Ryan Hensleigh, Desheng Yao, Deepam Maurya, Prashant Kumar, Min Gyu Kang, Shashank Priya, Xiaoyu Zheng, Three-dimensional printing of piezoelectric materials with designed anisotropy and directional response, Nat. Mater. 18 (3) (2019) 234–241.
[32] Pei Zhang, Iek Man Lei, Guangda Chen, Jingsen Lin, Xingmei Chen, Jiajun Zhang, Chengcheng Cai, Xiangyu Liang, Ji Liu, Integrated 3D printing of flexible electroluminescent devices and soft robots, Nat. Commun. 13 (1) (2022) 4775.
[33] Yijie Jiang, Md Nurul Islam, Rui He, Xiaozhou Huang, Peng-Fei Cao, Rigoberto C. Advincula, Narendra Dahotre, Pei Dong, H. Felix Wu, Wonbong Choi, Recent advances in 3D printed sensors: materials, design, and manufacturing, Adv. Mater. Technol. 8 (2) (2023) 2200492.
[34] Ying Hong, Biao Wang, Weikang Lin, Lihan Jin, Shiyuan Liu, Xiaowei Luo, Jia Pan, Wenping Wang, Zhengbao Yang, Highly anisotropic and flexible piezoceramic kirigami for preventing joint disorders, Sci. Adv. 7 (11) (2021) eabf0795.
[35] Huachen Cui, Desheng Yao, Ryan Hensleigh, Haotian Lu, Ariel Calderon, Zhenpeng Xu, Sheyda Davaria, Zhen Wang, Patrick Mercier, Pablo Tarazaga, et al., Design and printing of proprioceptive three-dimensional architected robotic metamaterials, Science 376 (6599) (2022) 1287–1293.
[36] Haotian Lu, Huachen Cui, Gengxi Lu, Laiming Jiang, Ryan Hensleigh, Yushun Zeng, Adnan Rayes, Mohanchandra K. Panduranga, Megha Acharya, Zhen Wang, et al., 3D printing and processing of miniaturized transducers with near-pristine piezoelectric ceramics for localized cavitation, Nat. Commun. 14 (1) (2023) 2418.
[37] Graeme W. Milton, Marc Briane, John R. Willis, On cloaking for elasticity and physical equations with a transformation invariant form, New J. Phys. 8 (10) (2006) 248.
[38] Andrew N. Norris, Alexander L. Shuvalov, Elastic cloaking theory, Wave Motion 48 (6) (2011) 525–538.
[39] Fernando Guevara Vasquez, Graeme W. Milton, Daniel Onofrei, Pierre Seppecher, Transformation elastodynamics and active exterior acoustic cloaking, in: Acoustic Metamaterials: Negative Refraction, Imaging, Lensing and Cloaking, Springer, 2013, pp. 289–318.
[40] Hussein Nassar, Q.-C. He, Nicolas Auffray, Willis elastodynamic homogenization theory revisited for periodic media, J. Mech. Phys. Solids 77 (2015) 158–178.
[41] Michele Brun, Sébastien Guenneau, Alexander B. Movchan, Achieving control of in-plane elastic waves, Appl. Phys. Lett. 94 (6) (2009).
[42] Hussein Nassar, Y.Y. Chen, G.L. Huang, A degenerate polar lattice for cloaking in full two-dimensional elastodynamics and statics, Proc. R. Soc. A 474 (2219) (2018) 20180523.
[43] Hussein Nassar, Y.Y. Chen, G.L. Huang, Isotropic polar solids for conformal transformation elasticity and cloaking, J. Mech. Phys. Solids 129 (2019) 229–243.
[44] H.K. Zhang, Yi Chen, X.N. Liu, G.K. Hu, An asymmetric elastic metamaterial model for elastic wave cloaking, J. Mech. Phys. Solids 135 (2020) 103796.
[45] Hussein Nassar, Y.Y. Chen, G.L. Huang, Polar metamaterials: a new outlook on resonance for cloaking applications, Phys. Rev. Lett. 124 (8) (2020) 084301.
[46] Xianchen Xu, Chen Wang, Wan Shou, Zongliang Du, Yangyang Chen, Beichen Li, Wojciech Matusik, Nassar Hussein, Guoliang Huang, Physical realization of elastic cloaking with a polar material, Phys. Rev. Lett. 124 (11) (2020) 114301.
[47] Shiheng Zhao, Jiaji Chen, Zheng Chang, Guoliang Huang, Microstructure realization of a lattice-based polar solid for arbitrary elastic waveguiding, J. Mech. Phys. Solids 173 (2023) 105226.
[48] Yangyang Chen, Michael R. Haberman, Controlling displacement fields in polar willis solids via gauge transformations, Phys. Rev. Lett. 130 (14) (2023) 147201.
[49] Yangyang Chen, Hussein Nassar, Guoliang Huang, Discrete transformation elasticity: An approach to design lattice-based polar metamaterials, Internat. J. Engrg. Sci. 168 (2021) 103562.
[50] René Pernas-Salomón, Gal Shmuel, Symmetry breaking creates electromomentum coupling in piezoelectric metamaterials, J. Mech. Phys. Solids 134 (2020) 103770.
[51] René Pernas-Salomón, Gal Shmuel, Fundamental principles for generalized willis metamaterials, Phys. Rev. Appl. 14 (6) (2020) 064005.
[52] René Pernas-Salomón, Michael R. Haberman, Andrew N. Norris, Gal Shmuel, The electromomentum effect in piezoelectric willis scatterers, Wave Motion 106 (2021) 102797.
[53] Kevin Muhafra, Michael R. Haberman, Gal Shmuel, Discrete one-dimensional models for the electromomentum coupling, Phys. Rev. Appl. 20 (1) (2023) 014042.
[54] Krzysztof K. Dudek, Julio A. Iglesias Martínez, Gwenn Ulliac, Laurent Hirsinger, Lianchao Wang, Vincent Laude, Muamer Kadic, Micro-scale mechanical metamaterial with a controllable transition in the Poisson's ratio and band gap formation, Adv. Mater. 35 (20) (2023) 2210993.
[55] Amin Farzaneh, Nikhil Pawar, Carlos M. Portela, Jonathan B. Hopkins, Sequential metamaterials with alternating Poisson's ratios, Nat. Commun. 13 (1) (2022) 1041.
[56] Yuhao Bao, Zishen Wei, Zhiyuan Jia, Dazhi Wang, Xiaopeng Zhang, Zhan Kang, Mechanical metamaterial design with the customized low-frequency bandgap and negative Poisson's ratio via topology optimization, Extrem. Mech. Lett. 67 (2024) 102124.
[57] Aoxi Wang, Zhiqiang Meng, Chang Qing Chen, Static topological mechanics with local resonance, J. Mech. Phys. Solids 190 (2024) 105705.
[58] Anne S. Meeussen, Giovanni Bordiga, Audrey X. Chang, Ben Spoettling, Kaitlyn P. Becker, L. Mahadevan, Katia Bertoldi, Textile hinges enable extreme properties of kirigami metamaterials, Adv. Funct. Mater. (2024) 2415986.